

A robust 2D shallow water model for solving flow over complex topography using homogenous flux method

M. Guan^{*,†}, N. G. Wright and P. A. Sleigh

School of Civil Engineering, University of Leeds, Leeds, LS2 9JT, UK

SUMMARY

A robust Godunov-type numerical scheme solver is proposed for solving 2D SWEs and is applied to simulate flow over complex topography with wetting and drying. In reality, the topography is usually complex and irregular; therefore, to avoid the numerical errors generated by such features, a Homogenous Flux Method is used to handle the bed slope term in the SWEs. The method treats the bed slope term as a flux to be incorporated into the flux gradient and so maintains the balance between the two in a Godunov-type shock-capturing scheme. The main advantages of the method are: first, it is simple and easy to implement; second, numerical experiments demonstrate that it can handle discontinuous or vertical bed topography without any special treatment and third, it is applicable to both steady and unsteady flows. It is demonstrated how the approach set out here can be applied to the nonlinear hyperbolic system of the SWEs. The two-dimensional hyperbolic system is then solved by use of a second-order total-variation-diminishing version of the weighted average flux method in conjunction with a Harten-Lax-van Leer-Contract approximate Riemann solver incorporating the new flux gradient term. Several benchmark tests are presented to validate the model and the approach is verified against experimental measurements from the European Union Concerted Action on Dam Break Modelling project. These show very good agreement. Finally, the method is applied to a volcano-induced outburst flood over an initially dry channel with complex irregular topography to demonstrate the technique's capability in simulating a real flood. Copyright © 2013 John Wiley & Sons, Ltd.

Received 24 October 2012; Revised 13 February 2013; Accepted 26 February 2013

KEY WORDS: shallow water equations; source terms; homogenous flux; wetting/drying; irregular topography; TVD-WAF/HLLC

1. INTRODUCTION

Numerical techniques for the solution of the SWEs that represent flow in rivers and estuaries have developed considerably since they were first adopted in the 70s [1–3], and their use has become widespread. Amongst the techniques used, those based on finite volume Godunov-type Riemann Solvers [4–6] are robust and accurate and have been used successfully in commercial as well as academic contexts. However, with these and other methods, the treatment of source terms and the numerical difficulties associated with wetting and drying are problematic, and in view of their influence on numerical accuracy, researchers have sought to overcome these with some success.

For the first of these issues, the source term treatment is critical for robust and accurate application of the finite volume method. This is especially true for the source terms relating to the bed geometry, because numerical errors will arise if an imbalance between the flux gradient and the bed slope source terms is created. To handle irregular bottom geometry, many approaches have been developed [7–11]. However, some limitations still exist in such methods. For example, Nujic's method [10] removed the $1/2 gh^2$ term in the flux gradient and combined it with the source term. This is simple but could not solve the problem completely and exhibited numerical errors. LeVeque's approach

*Correspondence to: M. Guan, University of Leeds, Leeds, UK.

†E-mail: cnmg@leeds.ac.uk, mingfu.guan@hotmail.com

[9] addressed the source term by introducing a Riemann problem in the centre of each cell whose flux difference exactly cancels the source term; however, the method is complicated to implement and is not always robust with numerical errors apparently in the case of unsteady state and steady transcritical flows with shocks. The upwind source term treatment from the Zaragoza school [7, 8] shows very robust and accurate solutions but at the cost of complexity in implementation. The surface gradient method (SGM) proposed by Zhou *et al.* [11] adopted a linear reconstruction of data in Monotone Upstream-centered Schemes for Conservation Laws-type scheme, which is applicable to steady and unsteady problems, but the steady flow simulation results are not as adequate as other methods, and additional special treatment must be implemented for the vertical bed step case [12].

Lee and Wright [13] presented a novel, simple and efficient technique for source term treatment in one-dimensional SWEs. They combined the source terms with the flux gradient to balance them and thereby derive a homogeneous form of equations, which is straightforward to solve. This method implicitly ensures that the source terms are discretised in balance with the flux terms without any additional treatment. Lee and Wright [13] presented several benchmarks using well-known Riemann solvers and showed very good agreement with analytical solutions. The advantages of this method lie in its simplicity, efficiency and range of applicability. The approach, however, was only described and demonstrated for one-dimensional modelling with first-order accuracy. The applicability of such a method to two-dimensional equations with second-order accuracy should also give significant advantages but has not been presented so far. In two-dimensional flows with complex, irregular topography, the wetting/drying problem is a frequent source of instability and inaccuracy. In solving nonlinear SWEs, this problem must be considered thoroughly, as small naturally-occurring water depths can cause unrealistic high velocities that will lead to numerical instabilities. A plethora of wetting/drying algorithms have been developed for the hyperbolic SWEs [6, 14–18]. For example, Toro's method [18] proposed shock-capturing schemes considering that a cell is dry if water depth is below a small critical value. Bradford and Sanders [16] suggested bypassing the incorrect estimation of pressure and body forces in partially wet cells by using Neumann extrapolation of the velocity. Brufau *et al.* [14] used an algorithm that modified the bed slope by enforcing the mass balance in the mass conservation equation, but it is only used for the first-order accurate scheme. Liang and Borthwick's approach [15] modified the mass conservation in both fully and partially submerged cells during flooding and recession. A straightforward wetting/drying treatment is described in this paper, and its application to a range of complex flows is demonstrated.

On the basis of the aforementioned issues outlined, the main objective of this study is to propose a robust source term treatment in 2D, the so-called Homogenous Flux Method (HFM) and thereby to develop a straightforward and efficient method for application to wet/dry fronts in irregular topography. We extend the homogenous source term treatment method of Lee and Wright [13] to two dimensions for aspects that do not arise in 1D, and the modified Godunov-type numerical schemes are defined. Following this, the approach to deal with wet/dry fronts is described, and several test case situations are analysed. Due to its simplicity and efficiency for shock-capturing problems with wet/dry fronts, the second-order total-variation-diminishing version of the weighted average flux method (TVD-WAF) discretisation in conjunction with the Harten-Lax-van Leer-Contract (HLLC) Riemann solver is adopted in this study. The scheme achieves second-order accuracy in space and time without performing data reconstruction.

2. GOVERNING EQUATIONS

2.1. Modified form of 2D SWEs

The hydrodynamic model is governed by the 2D SWEs on the basis of mass continuity and momentum balance. The diffusion terms, due to viscosity and turbulence, are not incorporated here but could be incorporated if necessary. In vector form, the equations can be expressed as follows:

$$\frac{\partial \mathbf{U}}{\partial t} + \frac{\partial \mathbf{F}}{\partial x} + \frac{\partial \mathbf{G}}{\partial y} = \mathbf{S}_o + \mathbf{S}_f, \quad (1)$$

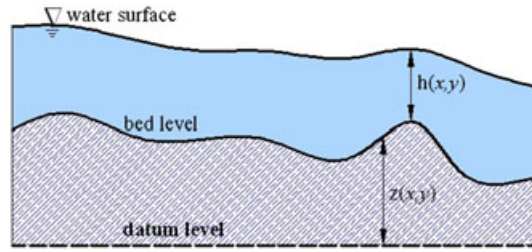


Figure 1. Sketch of shallow water over irregular bed.

$$\mathbf{U} = \begin{bmatrix} h \\ hu \\ hv \end{bmatrix} \quad \mathbf{F} = \begin{bmatrix} hu \\ hu^2 + \frac{1}{2}gh^2 \\ huv \end{bmatrix} \quad \mathbf{G} = \begin{bmatrix} hv \\ huv \\ hv^2 + \frac{1}{2}gh^2 \end{bmatrix} \quad \mathbf{S}_o = \begin{bmatrix} 0 \\ ghS_{ox} \\ ghS_{oy} \end{bmatrix} \quad \mathbf{S}_f = \begin{bmatrix} 0 \\ -ghS_{fx} \\ -ghS_{fy} \end{bmatrix},$$

where h represents the water depth (see Figure 1), g is the acceleration due to gravity and u and v denote the depth averaged velocity components in the x and y coordinates, respectively. S_{ox} , S_{oy} are the bed slopes in x -direction and y -direction, and S_{fx} , S_{fy} are friction slopes in x -direction and y -direction. They are defined by

$$S_{ox} = -\frac{\partial z_b}{\partial x}, S_{oy} = -\frac{\partial z_b}{\partial y}, \quad (2)$$

$$S_{fx} = \frac{n^2 u \sqrt{u^2 + v^2}}{h^{4/3}}, S_{fy} = \frac{n^2 v \sqrt{u^2 + v^2}}{h^{4/3}}, \quad (3)$$

in which z_b is the bed level at (x, y) location (see Figure 1) and the friction slopes S_{fx} , S_{fy} are defined on the basis of Manning's roughness coefficient denoted by n . The integral form of Equation (1) over a fixed volume Ω can be written by

$$\frac{\partial}{\partial t} \int_{\Omega} \mathbf{U} d\Omega + \int_{\Omega} (\nabla \cdot \mathbf{E}) d\Omega = \int_{\Omega} (\mathbf{S}_o + \mathbf{S}_f) d\Omega, \quad (4)$$

in which $\mathbf{E} = [\mathbf{F}, \mathbf{G}]^T$ is the flux tensor. The application of the Gauss's divergence theorem leads to the following conservation equation with surface integral:

$$\frac{\partial}{\partial t} \int_{\Omega} \mathbf{U} d\Omega + \oint_s (\mathbf{E} \cdot \mathbf{n}) ds = \int_{\Omega} (\mathbf{S}_o + \mathbf{S}_f) d\Omega, \quad (5)$$

where s represents the surface boundary of control area Ω , and \mathbf{n} is the outward pointing normal vector, $\mathbf{n} = [n_x, n_y]^T$. The Jacobian matrix, \mathbf{J}_n of the normal flux can be expressed by

$$\mathbf{J}_n = \frac{\partial (\mathbf{E} \cdot \mathbf{n})}{\partial \mathbf{U}} = \frac{\partial \mathbf{F}}{\partial \mathbf{U}} n_x + \frac{\partial \mathbf{G}}{\partial \mathbf{U}} n_y, \quad (6)$$

$$\mathbf{J}_n = \begin{bmatrix} 0 & n_x & n_y \\ (gh - u^2)n_x - uvn_y & vn_y + 2un_x & un_y \\ (gh - v^2)n_y - uvn_x & vn_x & un_x + 2vn_y \end{bmatrix}. \quad (7)$$

The system for the governing equation can be defined using an averaged Jacobian matrix $\tilde{\mathbf{J}}_n$ with eigenvalues and eigenvectors by

$$\tilde{\lambda}_1 = \tilde{u}n_x + \tilde{v}n_y - \tilde{c}, \tilde{\lambda}_2 = \tilde{u}n_x + \tilde{v}n_y, \tilde{\lambda}_3 = \tilde{u}n_x + \tilde{v}n_y + \tilde{c}, \quad (8)$$

$$\tilde{\mathbf{e}}_1 = \begin{pmatrix} 1 \\ \tilde{u} - \tilde{c}n_x \\ \tilde{v} - \tilde{c}n_y \end{pmatrix}, \tilde{\mathbf{e}}_2 = \begin{pmatrix} 1 \\ -\tilde{c}n_y \\ -\tilde{c}n_x \end{pmatrix}, \tilde{\mathbf{e}}_3 = \begin{pmatrix} 1 \\ \tilde{u} + \tilde{c}n_x \\ \tilde{v} + \tilde{c}n_y \end{pmatrix}, \quad (9)$$

in which \tilde{c} is the celerity of small amplitude surface waves. The average values at the interface are calculated as:

$$\tilde{u} = \frac{u_R \sqrt{h_R} + u_L \sqrt{h_L}}{\sqrt{h_R} + \sqrt{h_L}}, \tilde{v} = \frac{v_R \sqrt{h_R} + v_L \sqrt{h_L}}{\sqrt{h_R} + \sqrt{h_L}}, \tilde{c} = \sqrt{\frac{g(h_R + h_L)}{2}}, \tilde{h} = \sqrt{h_R h_L}, \quad (10)$$

where the subscripts L and R represent left and right side of the cell interface, and h_L and h_R denote water depth at the centre of left and right cell. In the hydrodynamic case, the source terms are combined into the bed slope term S_o and friction slope term S_f . Generally, the source term relevant to bottom geometry plays a significant role in maintaining flux balance [13]. Therefore, an approach addressing the bed slope term is adopted here by defining a bed slope source flux tensor, \mathbf{M} . More specifically, the bottom variation term S_o is quantified as a flux to be incorporated into flux terms, thereby automatically achieving the exact balance between flux gradient and bed slope. Thus,

$$\int_{\Omega} (\nabla \cdot \mathbf{M}) d\Omega = \int_{\Omega} \mathbf{S}_o d\Omega,$$

where \mathbf{M} is defined as bed slope source flux tensor, $\mathbf{M} = [\mathbf{B}_1, \mathbf{B}_2]^T$, and $\mathbf{B}_1, \mathbf{B}_2$ are the source flux vectors corresponding to the bed slope term in the x -direction and y -direction, respectively. So, the modified homogenous form of the two-dimensional SWEs can be obtained by incorporating bed slope source flux \mathbf{M} into flux terms \mathbf{E} and given by

$$\frac{\partial}{\partial t} \int_{\Omega} \mathbf{U} d\Omega + \int_{\Omega} [\nabla \cdot (\mathbf{E} - \mathbf{M})] d\Omega = \int_{\Omega} \mathbf{S}_f d\Omega.$$

So, system Equation (1) is rewritten by

$$\frac{\partial \mathbf{U}}{\partial t} + \frac{\partial \mathbf{H}}{\partial x} + \frac{\partial \mathbf{K}}{\partial y} = \mathbf{S}_f(x, y, \mathbf{U}), \quad (11)$$

in which $\mathbf{H} = \mathbf{F} - \mathbf{B}_1$ and $\mathbf{K} = \mathbf{G} - \mathbf{B}_2$ are the modified flux vectors, where $\mathbf{B}_1 = [0, R_1, 0]^T$ and $\mathbf{B}_2 = [0, 0, R_2]^T$; therein, R_1 is the source flux relevant to bed slope S_{ox} in x -direction and R_2 is the source flux relevant to bed slope S_{oy} in y -direction. Source term \mathbf{S}_f is the vector form relevant to friction component. Because the friction source term \mathbf{S}_f is not often the cause of the imbalance problem of shallow water model, a simple cell-centred pointwise method is used to discretise the friction vector \mathbf{S}_f in this study. On the basis of the aforementioned points, Figure 2 illustrates the fluxes at the corresponding cell interface.

Similarly, for the modified vector form of the 2D SWEs, the explicit finite volume discretisation method is adopted to discretise the modified 2D conservation equation.

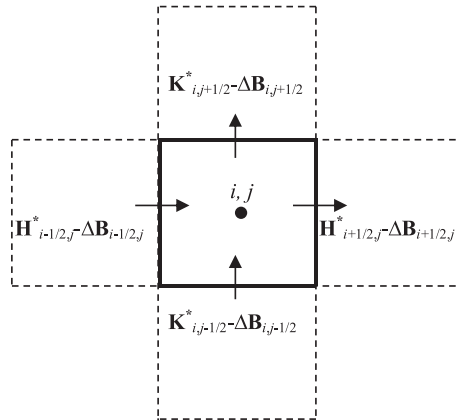


Figure 2. Fluxes inclusion of bed slope flux cross structural control cell.

For a structured grid, the updating of conservation variables (\mathbf{U}) is rewritten by

$$\mathbf{U}_{i,j}^{n+1} = \mathbf{U}_{i,j}^n - \frac{\Delta t}{\Delta x} (\mathbf{H}_{i+1/2,j}^* - \mathbf{H}_{i-1/2,j}^*) - \frac{\Delta t}{\Delta y} (\mathbf{K}_{i,j+1/2}^* - \mathbf{K}_{i,j-1/2}^*) + \Delta t \mathbf{S}_{f,i,j}, \quad (12)$$

in which \mathbf{H}^* and \mathbf{K}^* are the numerical flux at the interface between adjacent cells, Δt is the time interval, and Δx and Δy are the cell length in x -direction and y -direction.

2.2. Bed discretisation and source flux R_1 , R_2

The source flux terms R_1 and R_2 , which are the component of source flux vector \mathbf{B}_1 and \mathbf{B}_2 , are related only to the bed slope term. A definition of the flux term related to these bed slope term is required. The approach incorporates the bed slope term into the flux terms effectively; that is to say, the nonhomogenous form of system Equation (1) is converted to homogenous form for the bed slope source term. Thus, all the external forces caused by bed slope in a cell are exerted by the bed slope source flux at the interface of adjacent cells. To be compatible with this method, a proper bed reconstruction must be implemented. In this paper, the cell-centred piecewise linear bed reconstruction is applied to derive the bed slope source flux at the cell interface. Except for this, there is no need for any special treatment for the bed slope source term. Taking ΔR_1 as an example, the definition of the source flux R_1 can be obtained by the following approach. Comparing Equations (1) and (11), we can have:

$$\frac{\partial R_1}{\partial x} = -ghS_{ox} = -gh \frac{\partial z_b}{\partial x} = -gh \frac{\partial(\eta - h)}{\partial x}, \quad (13)$$

where z_b is the bed elevation at the cell centre, which is discretised by cell-centred approach, $\partial z_b / \partial x$ represents the slope of bed elevation at two adjacent cell centres, η is the water surface elevation and h is the water depth at the discretised cell. The difference of the source flux, ΔR_1 , at the boundary between the cell (i, j) and $(i + 1, j)$ can be obtained by integrating Equation (13) over the x -direction face of the two cells interface.

$$\int_{x_i}^{x_{i+1}} \frac{\partial R_1}{\partial x} dx = \int_{x_i}^{x_{i+1}} g \left(-h \frac{\partial \eta}{\partial x} + h \frac{\partial h}{\partial x} \right) dx, \quad (14)$$

in which x_i and x_{i+1} are the x -value of the i th and $i + 1$ th cell centre. For the two discretised cells here, Equation (14) is approximately rewritten by

$$\frac{\Delta R_1}{\Delta x} = -\frac{1}{2}g(h_{i,j} + h_{i+1,j}) \left(\frac{\eta_{i+1,j} - \eta_{i,j}}{\Delta x} \right) + \frac{1}{2}g \left(\frac{h_{i+1,j}^2 - h_{i,j}^2}{\Delta x} \right), \quad (15)$$

where $\eta_{i,j}$ and $\eta_{i+1,j}$ are the water surface elevations at the (i, j) and $(i + 1, j)$ cell centre. Therefore, in x -direction, ΔR_1 is then given by

$$\Delta R_{1(i+1/2,j)} = R_{1(i+1,j)} - R_{1(i,j)} = -\frac{1}{2}g(h_{i,j} + h_{i+1,j})\Delta\eta_{x(i+1/2,j)} + \frac{1}{2}g(h_{i+1,j}^2 - h_{i,j}^2), \quad (16)$$

where $\Delta\eta_{x(i+1/2,j)}$ represents the difference of water elevation at i th and $i + 1$ th cell centre in x -direction. Define $\mathbf{\Omega}_{ox(i+1/2,j)} = -0.5g(h_{i,j} + h_{i+1,j})\Delta\eta_{x(i+1/2,j)}$; Equation (16) is simplified as

$$\Delta R_{1(i+1/2,j)} = R_{1(i+1,j)} - R_{1(i,j)} = [\mathbf{\Omega}_{ox}]_{i+1/2,j} + \frac{1}{2}g(h_{i+1,j}^2 - h_{i,j}^2). \quad (17a)$$

Similarly, at the interface $i - 1/2$, the source term flux is written by

$$\Delta R_{1(i-1/2,j)} = R_{1(i,j)} - R_{1(i-1,j)} = [\mathbf{\Omega}_{ox}]_{i-1/2,j} + \frac{1}{2}g(h_{i,j}^2 - h_{i-1,j}^2). \quad (17b)$$

In Equation (17), the $\mathbf{\Omega}_{ox}$ term represents the momentum flux due to the water level difference in x -direction, and the second term $\Delta(\frac{1}{2}gh^2)$ represents the difference in the hydrostatic pressure

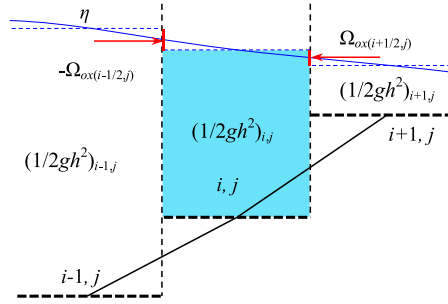


Figure 3. External force exerted by water surface elevation difference Ω_{ox} between two adjacent cells and hydrostatic pressure term $(1/2gh^2)$ in the cells.

term between left and right cells. Therefore, when splitting ΔR_1 , the first terms in Equations (17) are treated as an external force exerted by splitting between the neighbouring cells (see Figure 3), and the hydrostatic pressure term $\frac{1}{2}gh^2$ is split between each cell to balance the hydrostatic pressure term in the flux vectors. To update the variables at cell (i, j) , the source term R_1 in each neighbouring cell is calculated by:

$$R_{1(i-1,j)} = -[\Omega_{ox}]_{i-1/2,j} + \left(\frac{1}{2}gh^2\right)_{i-1,j} \quad (18a)$$

$$R_{1(i,j)} = \left(\frac{1}{2}gh^2\right)_{i,j} \quad (18b)$$

$$R_{1(i+1,j)} = [\Omega_{ox}]_{i+1/2,j} + \left(\frac{1}{2}gh^2\right)_{i+1,j} \quad (18c)$$

The momentum flux terms R_1, R_2 in each cell do not have an absolute value but a relative value. These three flux terms are calculated by decomposing Equations (17a) and (17b). In other words, when updating $\mathbf{U}_{i,j}$, Equations (18) are adopted; however, when updating $\mathbf{U}_{i+1,j}$, the source flux term $R_{1(i,j)}, R_{1(i+1,j)}$ and $R_{1(i+2,j)}$ are recomputed by a similar decomposition of $\Delta R_{1(i+1/2,j)}$ and $\Delta R_{1(i+3/2,j)}$. In fact, only the source term flux difference influences the updating \mathbf{U} vector. For example, the interface flux of Roe's scheme in the x -direction generally can be expressed by

$$\mathbf{H}_{i-1/2,j}^* = \frac{1}{2}[(\mathbf{F}_{i-1,j} - \mathbf{B}_{1(i-1,j)}) + (\mathbf{F}_{i,j} - \mathbf{B}_{1(i,j)})] - \tilde{\mathbf{J}}_n \Delta \mathbf{U}'_{i-1/2,j}, \quad (19a)$$

$$\mathbf{H}_{i+1/2,j}^* = \frac{1}{2}[(\mathbf{F}_{i,j} - \mathbf{B}_{1(i,j)}) + (\mathbf{F}_{i+1,j} - \mathbf{B}_{1(i+1,j)})] - \tilde{\mathbf{J}}_n \Delta \mathbf{U}'_{i+1/2,j}, \quad (19b)$$

where $\Delta \mathbf{U}'_{i\pm 1/2,j} = [\Delta h', \Delta(hu)', \Delta(hv)']^T_{i\pm 1/2,j}$ is the modified difference of \mathbf{U} . According to the updating equation (Equation (12)), it is necessary to calculate the difference of left and right interface in a cell by:

$$\begin{aligned} \mathbf{H}_{i+\frac{1}{2},j}^* - \mathbf{H}_{i-\frac{1}{2},j}^* &= \frac{1}{2}[(\mathbf{F}_{i+1,j} + \mathbf{F}_{i,j}) - (\mathbf{F}_{i-1,j} + \mathbf{F}_{i,j}) \\ &\quad - (\mathbf{B}_{1(i,j)} - \mathbf{B}_{1(i-1,j)}) - (\mathbf{B}_{1(i+1,j)} - \mathbf{B}_{1(i,j)})] \\ &\quad + \tilde{\mathbf{J}}_n \Delta \mathbf{U}'_{i-1/2,j} - \tilde{\mathbf{J}}_n \Delta \mathbf{U}'_{i+1/2,j} \\ &= \frac{1}{2}[(\mathbf{F}_{i+1,j} + \mathbf{F}_{i,j} - \Delta \mathbf{B}_{1(i+\frac{1}{2},j)}) - (\mathbf{F}_{i-1,j} + \mathbf{F}_{i,j} + \Delta \mathbf{B}_{1(i-\frac{1}{2},j)})] \\ &\quad + \tilde{\mathbf{J}}_n \Delta \mathbf{U}'_{i-1/2,j} - \tilde{\mathbf{J}}_n \Delta \mathbf{U}'_{i+1/2,j}, \end{aligned} \quad (20)$$

where $\Delta \mathbf{B}_{1(i-1/2,j)} = [0, \Delta R_{1(i-1/2,j)}, 0]^T$ and $\Delta \mathbf{B}_{1(i+1/2,j)} = [0, \Delta R_{1(i+1/2,j)}, 0]^T$ are the difference of source term flux vector in x -direction, and $\Delta R_{1(i-1/2,j)}$ and $\Delta R_{1(i+1/2,j)}$ can be calculated by use of Equations (17a) and (17b). Therefore, the relative decomposed source term flux in Equations (18) is sufficient for the solution of the scheme. For other numerical schemes, this is easily proving that. Similarly, in y -direction, the flux term R_2 is calculated by

$$R_{2(i,j-1)} = -[\Omega_{oy}]_{i,j-1/2} + \left(\frac{1}{2}gh^2\right)_{i,j-1} \quad (21a)$$

$$R_{2(i,j)} = \left(\frac{1}{2}gh^2\right)_{i,j} \quad (21b)$$

$$R_{2(i,j+1)} = [\Omega_{oy}]_{i,j+1/2} + \left(\frac{1}{2}gh^2\right)_{i,j+1} \quad (21c)$$

3. NUMERICAL MODEL

3.1. Numerical scheme

A wide range of numerical schemes have been proposed and an excellent review was written by Toro [18]. In this section, we take the modified equations with the source term fluxes and implement the first-order HLLC scheme. Further, the second-order TVD-WAF is applied. The intercell flux is obtained from an integral average of the flux function \mathbf{E} across the complete wave structure of the local Riemann problem with piecewise constant data $(\mathbf{U}_L, \mathbf{U}_R)$ [19–21]. A similar derivation method can be applied for other solvers.

3.1.1. The HLLC solver including the source flux. The HLLC approximate Riemann solver is a modification of the basic Harten, Lax, van Leer (HLL) scheme that accounts for the influence of intermediate waves [18] and ensures greater accuracy. In the structure of HLLC solver, there are two distinct fluxes for the star region (see Figure 4), so we need to determine the intermediate waves as well as from the left and right wave speed estimates.

First, we derive the modified intercell numerical flux vector \mathbf{E}^* with the incorporation of source fluxes as:

$$\mathbf{E}_{LR}^* = \begin{cases} \mathbf{E}_L & \text{if } S_L \geq 0 \\ \mathbf{E}_{*L} & \text{if } S_L < 0 \leq S_* \\ \mathbf{E}_{*R} & \text{if } S_* < 0 \leq S_R \\ \mathbf{E}_R & \text{if } S_R < 0 \end{cases}, \quad (22)$$

where $\mathbf{E}_L = \mathbf{E}(\mathbf{U}_L, \mathbf{B}_L)$ and $\mathbf{E}_R = \mathbf{E}(\mathbf{U}_R, \mathbf{B}_R)$ are the flux and conserved variable vectors at the left and right side of each cell interface, and \mathbf{E}_{*L} and \mathbf{E}_{*R} are the left and right numerical fluxes in the star region divided by middle wave S_* . We note that the intermediate wave arising from the presence of the tangential momentum equation is always a shear wave, across which the tangential

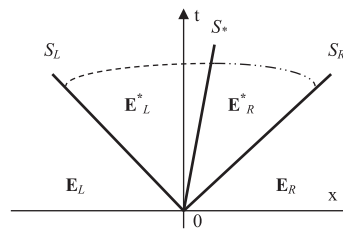


Figure 4. The structure of HLLC Riemann solver.

velocity component changes discontinuously, whereas the perpendicular velocity component and the water depth remain constant [18]. Taking calculation fluxes \mathbf{H}_{*L} and \mathbf{H}_{*R} in the x -direction as an example, they are calculated according to the following expressions:

$$\mathbf{H}_{*L} = \begin{bmatrix} H_{*1} \\ H_{*2} \\ v_L H_{*1} \end{bmatrix}, \mathbf{H}_{*R} = \begin{bmatrix} H_{*1} \\ H_{*2} \\ v_R H_{*1} \end{bmatrix}, \quad (23)$$

where v_L and v_R are the initial velocity tangential to the interface of a local Riemann problem, which remain unchanged across the left and right waves, respectively. $[H_{*1}, H_{*2}, H_{*3}]^T = \mathbf{H}_*$ is the flux in the star region according to the modified HLL formula when evaluating fluxes in the x -direction. For the y -direction, a similar approach is applied. The modified HLL formula is calculated by the following equation in two dimensions.

$$\mathbf{E}_* \cdot \mathbf{n} = \frac{S_R \mathbf{E}_L \cdot \mathbf{n} - S_L \mathbf{E}_R \cdot \mathbf{n} + S_R S_L \Delta \mathbf{U}'_{LR}}{S_R - S_L}, \quad (24)$$

in which the subscripts L and R represent the right and the left side of the cell interface, respectively; the S_L and S_R denote two wave speeds, which are supposed to be selected carefully to avoid entropy violation. Einfeldt's method [22] was adopted here, including dry bed options from the two rarefaction-approximate Riemann solver, and Roe's average eigenvalues were used. These are expressed by

$$S_L = \begin{cases} \min \left(\mathbf{q}_L \cdot \mathbf{n} - \sqrt{gh_L}, \tilde{\mathbf{u}}_{\perp} \cdot \mathbf{n} - \sqrt{g\tilde{h}} \right) & \text{if } h_L > 0 \\ \mathbf{q}_R \cdot \mathbf{n} - 2\sqrt{gh_R} & \text{if } h_L = 0 \end{cases}, \quad (25a)$$

$$S_R = \begin{cases} \min \left(\mathbf{q}_R \cdot \mathbf{n} + \sqrt{gh_R}, \tilde{\mathbf{u}}_{\perp} \cdot \mathbf{n} + \sqrt{g\tilde{h}} \right) & \text{if } h_R > 0 \\ \mathbf{q}_L \cdot \mathbf{n} + 2\sqrt{gh_L} & \text{if } h_R = 0 \end{cases}, \quad (25b)$$

in which $\mathbf{q} = [u, v]$, $\tilde{\mathbf{u}}_{\perp} = [\tilde{u}, \tilde{v}]$ is Roe's average velocity, and $\sqrt{g\tilde{h}}$ is Roe's average wave speed. The middle wave speed S_* can be calculated in a variety of ways, but the following form is recommended by Toro [18]:

$$S_* = \frac{S_L h_R (\mathbf{q}_R \cdot \mathbf{n} - S_R) - S_R h_L (\mathbf{q}_L \cdot \mathbf{n} - S_L)}{h_R (\mathbf{q}_R \cdot \mathbf{n} - S_R) - h_L (\mathbf{q}_L \cdot \mathbf{n} - S_L)}. \quad (26)$$

For the original HLL or HLLC scheme, $\Delta \mathbf{U}'$ in Equation (24) should be equal to $\mathbf{U}_R - \mathbf{U}_L$, representing the conserved variables difference between left and right cell; however, the $\Delta \mathbf{U}'$ becomes the net difference of conserved variables considering the bed geometry effect in this HFM because of the inclusion of source flux into flux term \mathbf{F} . Therefore, the modified $\Delta \mathbf{U}'$ must be recalculated. According to Equation (6) $\mathbf{J}_n = \frac{\partial(\mathbf{E} \cdot \mathbf{n})}{\partial \mathbf{U}}$, the flux difference is expressed by the Jacobian matrix multiplying the conserved variables' difference as $\Delta \mathbf{E} \cdot \mathbf{n} = \mathbf{J}_n \Delta \mathbf{U}$. For Roe's approximate Riemann solver, an approximate Jacobian $\tilde{\mathbf{J}}_{LR}$ at the edges of cell, analogous to \mathbf{J}_n , was constructed to satisfy the conservation property across discontinuities $\Delta \mathbf{E}_{LR} \cdot \mathbf{n} = \tilde{\mathbf{J}}_{LR} \Delta \mathbf{U}$, where $\tilde{\mathbf{J}}_{LR}$ is expressed by its eigenvalues. However, the solution structure of the HLL approximate Riemann solver is different from that of Roe's solver. To satisfy the conservation property for the HLL solver, the approximate Jacobian \mathbf{J}_{LR}^{HLL} is approximately constructed on the basis of Roe's Jacobian matrix by using the two alternative eigenvalues S_L and S_R calculated by Einfeldt's method [22], which is based on Roe's average eigenvalues. So the modified vector of $\Delta \mathbf{U}'$ satisfies the following equation:

$$\Delta \mathbf{E}_{LR} \cdot \mathbf{n} = \mathbf{J}_{LR}^{HLL} \Delta \mathbf{U}', \quad (27)$$

where $\Delta \mathbf{U}' = [\Delta h', \Delta(hu)', \Delta(hv)']_{LR}^T$ is the difference of the modified conservative variables between two adjacent cells and $\Delta \mathbf{E}_{LR}$ denotes the difference of flux vector inclusion of bed slope flux at the cell interface. More specifically, the Equation (27) is rewritten by:

$$\begin{bmatrix} \Delta(hu)n_x + \Delta(hv)n_y \\ \Delta(hu^2) + \Delta(gh^2/2)n_x + \Delta(huv)n_y \\ \Delta(huv)n_x + \Delta(hv^2) + \Delta(gh^2/2)n_y \end{bmatrix}_{LR} - \begin{bmatrix} 0 \\ \Delta R_1 n_x \\ \Delta R_2 n_y \end{bmatrix}_{LR} = \mathbf{J}_{LR}^{HLL} \begin{bmatrix} \Delta h' \\ \Delta(hu)' \\ \Delta(hv)' \end{bmatrix}_{LR}. \quad (28)$$

To calculate the flux in x -direction, $n_x = 1$ and $n_y = 0$. As mentioned before, the Jacobian matrix for HLL approximate Riemann solver, \mathbf{J}_{LR}^{HLL} constructed by using the two eigenvalues S_L and S_R , is used instead of Roe's Jacobian matrix $\tilde{\mathbf{J}}_n$, referring to Lee and Wright [13]

$$\mathbf{J}_{LR}^{HLL} = \begin{bmatrix} 0 & 1 & 0 \\ -S_L S_R & S_L + S_R & 0 \\ -1/2(S_L + S_R)\tilde{v} & \tilde{v} & 1/2(S_L + S_R) \end{bmatrix}. \quad (29)$$

Putting Equation (29) into Equation (28) and solving it, the unknown conserved variable differences $\Delta h'$, $\Delta(hu)'$ and $\Delta(hv)'$ are derived as

$$\Delta h'_{LR} = -\frac{\Delta(hu^2)_{LR} - \Omega_{ox} - (S_L + S_R)\Delta(hu)_{LR}}{S_L S_R}, \quad (30a)$$

$$\Delta(hu)'_{LR} = \Delta(hu)_{LR}, \quad (30b)$$

$$\Delta(hv)'_{LR} = \Delta(hv)_{LR} + \tilde{v}(\Delta h'_{LR} - \Delta h_{LR}), \quad (30c)$$

where Ω_{ox} is the momentum flux due to water surface difference between left and right cells in the x -direction. Similarly, for the calculation of the flux in y -direction, $n_x = 0$ and $n_y = 1$. Putting n_x and n_y into Equation (28) and solving it, $\Delta h'$, $\Delta(hu)'$ and $\Delta(hv)'$ are expressed as

$$\Delta h'_{LR} = -\frac{\Delta(hv^2)_{LR} - \Omega_{oy} - (S_L + S_R)\Delta(hv)_{LR}}{S_L S_R}, \quad (31a)$$

$$\Delta(hu)'_{LR} = \Delta(hu)_{LR} + \tilde{\mathbf{u}}(\Delta h'_{LR} - \Delta h_{LR}), \quad (31b)$$

$$\Delta(hv)'_{LR} = \Delta(hv)_{LR}, \quad (31c)$$

where Ω_{oy} is the momentum flux due to water surface difference between left and right cells in y -direction. Overall, the modified difference of conservative terms $\Delta \mathbf{U}'$ can be summarised by incorporating n_x , n_y into the derived expressions; therefore, the new equations are rewritten by

$$\Delta h'_{LR} = -\frac{\Delta(h\mathbf{u}^2 \cdot \mathbf{n})_{LR} - \Omega \cdot \mathbf{n} - (S_L + S_R)[\Delta(h\mathbf{u} \cdot \mathbf{n})_{LR}]}{S_L S_R}, \quad (32a)$$

$$\Delta(hu)'_{LR} = \Delta(hu)_{LR} + \tilde{\mathbf{u}}(\Delta h'_{LR} - \Delta h_{LR}) \cdot n_y, \quad (32b)$$

$$\Delta(hv)'_{LR} = \Delta(hv)_{LR} + \tilde{v}(\Delta h'_{LR} - \Delta h_{LR}) \cdot n_x, \quad (32c)$$

in which $\mathbf{u}^2 = [u^2, v^2]$, $\Omega = [\Omega_{ox}, \Omega_{oy}]$, $\mathbf{u} = [u, v]$ and $\mathbf{n} = [n_x, n_y]^T$.

In general, it is vital that a scheme satisfies the C -property to maintain the correct balance between source terms and flux gradients. The C -property is the requirement for a well-balanced scheme [7, 23–25] and can be proved as follows (taking x -direction as an example). In case of no flow

$$\eta = h + z_b \equiv \text{constant value}, \quad \Delta \eta \equiv 0, u \equiv 0, S_{fx} \equiv 0.$$

Therefore, the external force due to water surface difference $\mathbf{\Omega}_{ox}$ is equivalent to zero and $R_{1(i-1,j)} = (\frac{1}{2}gh^2)_{i-1,j}$, $R_{1(i,j)} = (\frac{1}{2}gh^2)_{i,j}$, $R_{1(i+1,j)} = (\frac{1}{2}gh^2)_{i+1,j}$ in Equations (18). Putting the $\mathbf{\Omega}_{ox} \equiv 0$ and $u \equiv 0$ into Equation (30), the modified vector of $\mathbf{\Delta U}'$ satisfies $\mathbf{\Delta U}' \equiv \mathbf{0}[\Delta h' \equiv 0, \Delta(hu)' \equiv 0, \Delta(hv)' \equiv 0]$. Therefore, the momentum flux change at the cell (i, j) in x -direction is calculated by

$$\begin{aligned} H_m &= H_{i+1/2,j}^* - H_{i-1/2,j}^* \\ &= \frac{1}{2} \{ [(f_{i+1,j} - R_{1(i+1,j)}) + (f_{i,j} - R_{1(i,j)})] - [(f_{i,j} - R_{1(i,j)}) + (f_{i-1,j} - R_{1(i-1,j)})] \} \\ &= \frac{1}{2} \left\{ \left[\left(\frac{1}{2}gh_{i+1,j}^2 - \frac{1}{2}gh_{i+1,j}^2 \right) + \left(\frac{1}{2}gh_{i,j}^2 - \frac{1}{2}gh_{i,j}^2 \right) \right] \right. \\ &\quad \left. - \left[\left(\frac{1}{2}gh_{i,j}^2 - \frac{1}{2}gh_{i,j}^2 \right) + \left(\frac{1}{2}gh_{i-1,j}^2 + \frac{1}{2}gh_{i-1,j}^2 \right) \right] \right\} \\ &\equiv 0. \end{aligned} \quad (33)$$

Similarly, in the y -direction, the momentum flux change at the cell (i, j) has

$$K_m = K_{i+1/2,j}^* - K_{i-1/2,j}^* \equiv 0. \quad (34)$$

Therefore, the conserved variables (\mathbf{U}) are updated at the new time by

$$\begin{aligned} \mathbf{U}_{i,j}^{n+1} &= \mathbf{U}_{i,j}^n - \frac{\Delta t}{\Delta x} (\mathbf{H}_{i+\frac{1}{2},j}^* - \mathbf{H}_{i-\frac{1}{2},j}^*) - \frac{\Delta t}{\Delta y} (\mathbf{K}_{i,j+\frac{1}{2}}^* - \mathbf{K}_{i,j-\frac{1}{2}}^*) + \Delta t \mathbf{S}_{f,i,j} \\ &= \mathbf{U}_{i,j}^n - 0 - 0 + 0 = \mathbf{U}_{i,j}^n. \end{aligned} \quad (35)$$

As shown previously in the text, the numerical solution of the stationary flow problem by the proposed scheme is equal to the exact solution where the flow variables do not change with time, that is, the initial state is maintained. From the previous analysis, the C -property is guaranteed by the proposed source term treatment method. The bed slope source term is therefore well-balanced with the flux gradient terms.

3.1.2. Second-order TVD-WAF scheme. To compute the intercell numerical fluxes, we employed the WAF method. However, the basic WAF scheme without TVD modification is seldom used in practice because of its unphysical oscillations so to avoid such oscillations, a TVD constraint is enforced on the WAF scheme with a flux limiter function. The TVD-WAF scheme is second-order accurate in space and time. A detailed description can be found in Toro [18]. The modified TVD-WAF scheme applied in this paper is described using the x -direction flux as an example; the y -direction is treated in similar way. The modified TVD-WAF flux can be written as:

$$\begin{aligned} \mathbf{H}_{i+1/2}^* &= \frac{1}{2} (\mathbf{H}_i + \mathbf{H}_{i+1}) - \frac{1}{2} \sum_{k=1}^N \text{sign}(c_k) \Phi_{i+1/2}^k \Delta \mathbf{H}_{i+1/2}^k \\ \text{sign}(a) &= \begin{cases} 1 & a > 0 \\ 0 & a = 0 \\ -1 & a < 0 \end{cases}, \end{aligned} \quad (36)$$

in which $\mathbf{H}_i = \mathbf{H}(\mathbf{U}_i, \mathbf{B}_i)$ and $\mathbf{H}_{i+1} = \mathbf{H}(\mathbf{U}_{i+1}, \mathbf{B}_{i+1})$ are the flux and conservative variable vectors at the left and right side of each cell interface, c_k is the Courant number for wave k , $c_k = \Delta t S_k / \Delta x$, S_k is the speed of wave k and N is the number of waves in the solution of the Riemann problem, $N = 3$, in conjunction with HLLC approximate Riemann solver. $\Delta \mathbf{H}_{i+1/2}^{(k)} = \mathbf{H}_{i+1/2}^{(k+1)} - \mathbf{H}_{i+1/2}^{(k)}$, which is the flux jump across wave k and $\mathbf{H}_{i+1/2}^{(k)}$ is the value of the flux vector in the interval k ; herein, $\mathbf{H}_{i+1/2}^{(1)} = \mathbf{H}(\mathbf{U}_i, \mathbf{B}_i)$, $\mathbf{H}_{i+1/2}^{(2)} = \mathbf{H}(\mathbf{U}_i^*, \mathbf{B}_i)$, $\mathbf{H}_{i+1/2}^{(3)} = \mathbf{H}(\mathbf{U}_{i+1}^*, \mathbf{B}_{i+1})$ and

$\mathbf{H}_{i+1/2}^{(4)} = \mathbf{H}(\mathbf{U}_{i+1}, \mathbf{B}_{i+1})$, which are estimated by virtue of the modified HLLC approximate Riemann solver, $\Phi(r)$ is the WAF limiter function. There are various limiter functions available to choose from [18]. The one used is the *minmod* limiter:

$$\Phi(r^k) = 1 - (1 - |c|)\phi(r^k)$$

$$\phi(r^k) = \max[0, \min(1, r^k)] \text{ (minmod limiter),}$$

where r^k is the ratio of the upwind change to the local change in scalar quantity q , which can be written:

$$r^k = \begin{cases} \frac{\Delta q_{i-1/2}^{(k)}}{\Delta q_{i+1/2}^{(k)}} = \frac{q_i^{(k)} - q_{i-1}^{(k)}}{q_{i+1}^{(k)} - q_i^{(k)}} & \text{if } c_k > 0 \\ \frac{\Delta q_{i+3/2}^{(k)}}{\Delta q_{i+1/2}^{(k)}} = \frac{q_{i+2}^{(k)} - q_{i+1}^{(k)}}{q_{i+1}^{(k)} - q_i^{(k)}} & \text{if } c_k < 0 \end{cases}. \quad (37)$$

For the x -direction two-dimensional SWEs, we choose $q = h$ for the nonlinear waves (waves S_L , $k=1$ and S_R , $k=3$) and $q = v$ the tangential velocity component for the shear wave (waves S_* , $k=2$).

3.2. Stability criteria

The numerical scheme is explicit, so to maintain stability, the well-known *CFL* stability condition is applied [26–28]. For a two-dimensional Cartesian cell, the time step Δt is determined by multiplying the Courant number by the smaller value of the time steps in x -direction and y -direction. This is expressed as

$$\Delta t = CFL \min \left(\min \frac{dx_i}{|u_i| + \sqrt{gh_i}}, \min \frac{dy_j}{|v_j| + \sqrt{gh_j}} \right),$$

where the Courant number $0 < CFL < 1$.

4. WETTING AND DRYING

At the wetting and drying front, small water depths can cause unrealistically high velocity, which in turn causes numerical instabilities. To overcome this, we introduced a water depth tolerance. If the water depth is smaller than the tolerance depth, it will be treated as a dry bed case whose velocity is set equal to zero; otherwise, it is treated as a wet bed case. In addition, the source term is incorporated into flux term, so when handling wet/dry fronts, the source term flux should be considered. According to the treatment of wetting and drying mentioned above, four wetting and drying situations are accounted for and they are summarised in Figure 5.

Most hydraulic conditions can be included in these four situations. More specifically,

- (1) Both left and right cell are dry (Figure 5a). The flux is considered as zero.
- (2) Both left and right cell are wet (Figure 5b). The numerical flux at cell interface is calculated according to the proposed numerical scheme without any special treatment.
- (3) One side cell is wet, another side cell is dry, and the relation of the water surface elevation and the bed elevation satisfies: $z_{bR} \geq \eta_L$ or $z_{bL} \geq \eta_R$ (Figure 5c). The flow flux at cell interface should be regarded as zero, but the source flux must still be calculated because it will be applied to balance the source flux at the former cell interface when updating the variables at the left cell. In this circumstance, a water elevation η'_R at dry cell is temporarily replaced; otherwise, a nonphysical flux will be predicted. The treatment is handled as:

$$\eta_R = z_{bR},$$

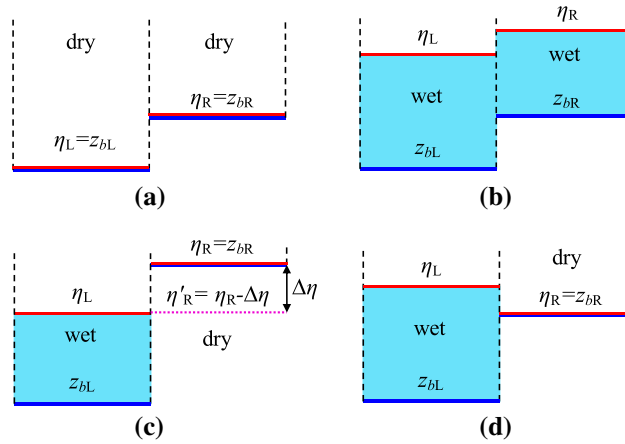


Figure 5. The scenarios of flow over variable topography.

$$\Delta\eta = \eta_R - \eta_L,$$

$$\eta'_R = \eta_R - \Delta\eta.$$

And meanwhile, the wet cell component normal to the dry cell interface is set to zero to ensure that the flow is stationary.

- (4) One side cell is wet, another side cell is dry, and the relation of the water surface elevation and the bed elevation satisfies: $z_{bR} < \eta_L$ or $z_{bL} < \eta_R$ (Figure 5d). No special treatment is carried out, and the cell interface flux will be in wet to dry direction according to the proposed numerical scheme.

Furthermore, updating the water depth at each time step may cause a negative value to occur, which violates mass conservation and will lead to a gain of mass. Therefore, a special treatment is required. In this paper, an acceptable method [14, 15] is applied to maintain mass conservation. First, the velocity components are treated as zero for any dry cells. In general, water is subtracted from the adjacent cell having most water, where the conserved variables hu and hv are modified so that u and v remain the same as before to maintain the front velocity components; if there is no adjacent cell to provide adequate water to be subtracted, then the negative mass of water for maintaining conservation is taken into the calculation at the next step, and meanwhile, this cell is regarded as drying until the cell is sufficiently recharged or a neighbour having adequate water is identified [15].

5. RESULTS AND DISCUSSIONS

In this section, several well-known benchmark cases are used to validate the proposed scheme. All the tests are undertaken using the TVD-WAF / HLLC scheme previously described. To demonstrate the proposed model's ability to deal with source terms as well as wetting/drying, we selected the following benchmark tests and application cases.

5.1. Still water over two smooth bumps

To verify that the proposed scheme can satisfy the C -property and achieve the correct balance between the flux term and source term with wet/dry fronts, we reproduced a test of still water over two smooth bumps. Similar tests with one submerged bump have been investigated in one dimension and two dimensions by other researchers [29–31]. In this test, two frictionless bumps are constructed, the centre of the submerged one is located at the $(x = 0.7 \text{ m}, y = 0.5 \text{ m})$, and the centre of the emerged one is located at $(x = 0.2 \text{ m}, y = 0.5 \text{ m})$. The whole container is $1 \times 1 \text{ m}$ square,

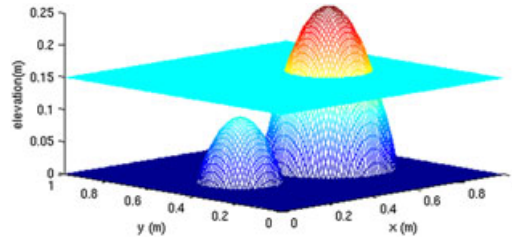


Figure 6. Still water over two smooth bumps: simulated water surface after 500 s.

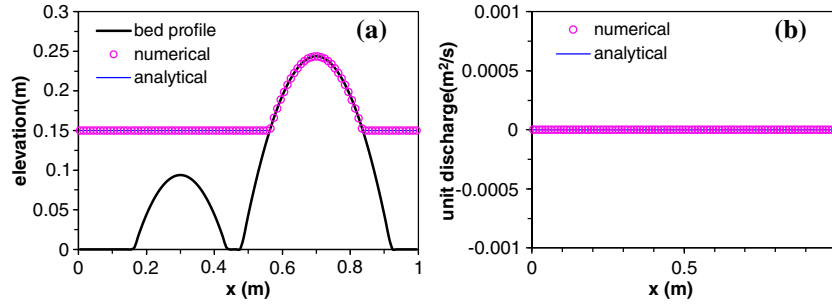


Figure 7. The comparison between numerical and analytical solutions at section $y = 0.5$ m after 500 s: (a) water elevation; (b) unit discharge.

with the bed elevation given by

$$z_b = \begin{cases} \max \left\{ 0, 0.25 - 5.0 \left[(x - 0.7)^2 + (y - 0.5)^2 \right] \right\} & x > 0.45m \\ \max \left\{ 0, 0.1 - 10.0 \left[(x - 0.3)^2 + (y - 0.5)^2 \right] \right\} & x \leq 0.45m \end{cases}$$

The initial water level is set as 0.15 m; so the initial water depth $h(x, y) = \max(0, 0.15 - z_b)$; both velocities in x -direction and y -direction are zero. Because there are no external forces, the water should keep still during the simulation period. The area is discretised by 100×100 cells ($\Delta x = \Delta y = 0.01$ m), and the simulation is carried out for 500 s. Figure 6 demonstrates the simulated water surface over the two bumps. To show the difference between numerical and exact solutions, Figure 7 illustrates the water level and unit discharge comparison with exact solutions at section $y = 0.5$ m. The results show that the proposed model maintains tranquil water perfectly and the water level and unit discharge are exactly reproduced, irrespective of whether the domain is wet or dry. This test verifies the well-balanced property of the proposed approach.

5.2. Steady flow over a bump

This test has been used by a range of authors for validating the treatment of bed slope source term [6, 11, 15, 32–34]. To verify that the proposed scheme achieves the correct balance between source flux and flux gradient, we also investigate a nonstationary steady state case. This is a one-dimensional test case but tested in two dimensions here, in which the spatial domain is represented by a 25×1 m rectangular, frictionless channel and then the computational domain is discretised into 250×10 cells. The bed profile is:

$$z_b = \begin{cases} 0.2 - 0.05(x - 10)^2 & 8 \leq x \leq 12 \\ 0 & \text{otherwise} \end{cases}$$

For the convergence of numerical solution, the global relative error $R < 1 \times 10^{-6}$ is defined here, where R is expressed by

$$R = \sqrt{\sum_i \left(\frac{h_i^n - h_i^{n-1}}{h_i^n} \right)^2}$$

where h_i^n and h_i^{n-1} are water depths at current and previous time steps at cell i .

Initial flow conditions for transcritical flow case are defined as: upstream inflow is equal to $0.18 \text{ m}^3/\text{s}$ and the downstream level is set equal to a constant 0.33 m . The initial water level is 0.33 m and the initial discharge is set to $0 \text{ m}^3/\text{s}$. To show how the proposed scheme performs, we present results by using the method proposed in this paper, which we will refer to as the HFM, using the well-balanced scheme proposed by Song *et al.* [17] and using SGM [11], which has been shown to handle this problem well and has been widely applied in solving the SWEs. The computed results are displayed in Figure 8 and show an excellent agreement between numerical results of water elevation, discharge and Froude number by the HFM and analytical results. Errors are only apparent for discharge at one point, whereas at others, values are as predicted analytically—something which is not achieved by any of the other methods for this test. The HFM gives better results than those of from the method of Song *et al.* [17] and SGM for discharge.

For the subcritical flow case, initial flow conditions are defined as: upstream inflow equal to $4.42 \text{ m}^3/\text{s}$ and downstream level equal to a constant 2 m . The computational results are shown in Figure 9. The comparisons between numerical solutions of the HFM and analytical solutions show almost exact agreement; both the SGM and the well-balanced method proposed by Liang and Borthwick [15] have a small oscillation in discharge around the bump [11], a similar or more severe oscillation also occurs on the test in other works [17, 35]. Figure 10 plotted relative error R against iteration number, demonstrating the convergence history of subcritical flow over a bump. The comparison highlights the capability of the proposed method in maintaining the balance between flux gradient and bed slope for nonstationary steady state flow.

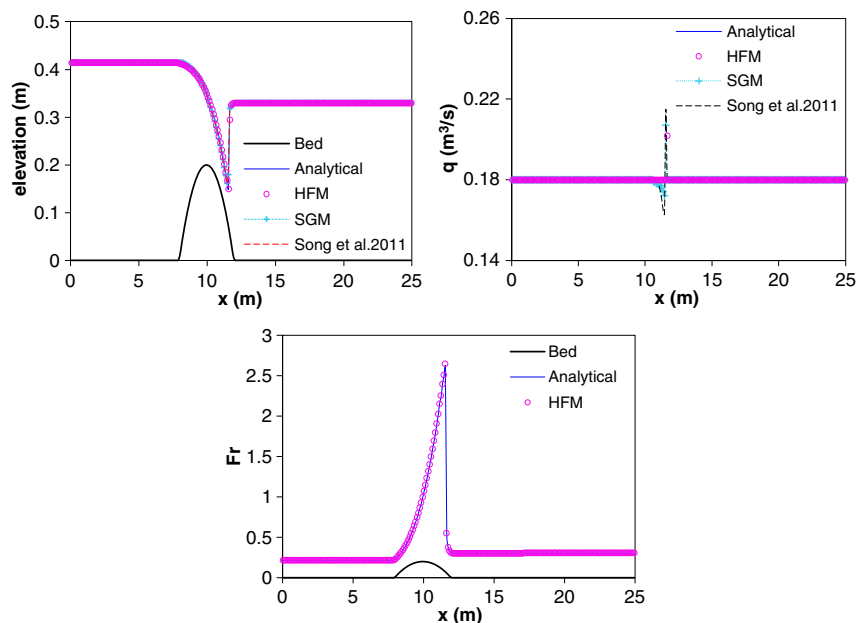


Figure 8. Transcritical flow over a bump: (a) water surface elevation, (b) discharge, (c) Froude number.

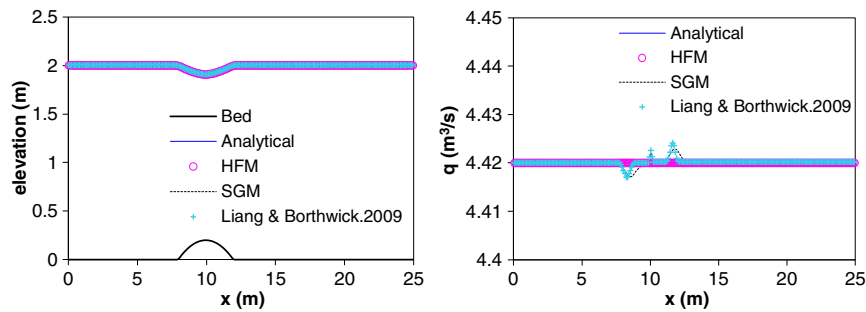


Figure 9. Subcritical flow over a bump.

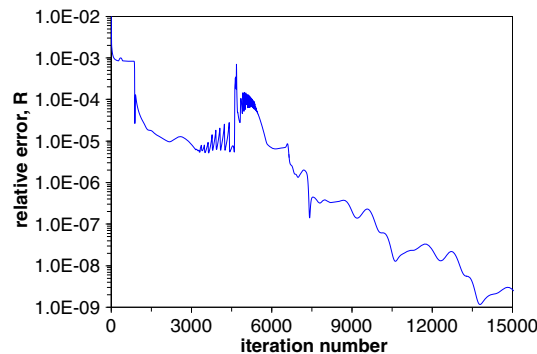


Figure 10. Subcritical flow over a bump: Convergence history.

5.3. Surge wave propagation crossing a vertical step

This case has been proposed and implemented by a number of researchers [12, 36] to test source term treatments with a vertical or discontinuous bed step. Although some treatment approaches for this have been proposed, few involve the treatment of the vertical bed step where significantly inaccurate results can occur. The flow conditions are defined as follows: the flow is unsteady; the channel length is 10,000 m and the bed step is 2 m in height at $x \geq 5000$ m, otherwise, the bed level is zero; and water surface elevation is 5.0 m in the channel; at the entrance, the water depth is imposed as a constant 10 m and the surge velocity is defined as

$$u(t) = (\eta_u - \eta_d) \sqrt{\frac{g(\eta_u - \eta_d)}{2\eta_u\eta_d}},$$

where η_u is the upstream water level of 10 m, and η_d represents the downstream water level of 5 m. The simulation was undertaken with 1000 uniform cells ($\Delta x = 10$ m). As before, we compare the numerical results with SGM, without additional special treatment at the vertical step. Figure 11 shows the comparisons of water surface and velocity between numerical solutions and analytical solutions [36] at $t = 600.5$ s. The comparisons show that the proposed method achieves good agreement with the analytical solution. However, there is an oscillation in the location of vertical step for SGM if it is not specially treated as described by Zhou *et al.* [12]. The oscillation causes the water elevation to be too large before the step location and smaller just after the step location when compared with the analytical solution (see Figure 11). Correspondingly, the velocity is smaller than HFM and analytical solutions. However, there is not a big discrepancy in the surge wave and water front position. The comparison indicates that the treatment in this study is more accurate and performs better than SGM for a discontinuous bed.

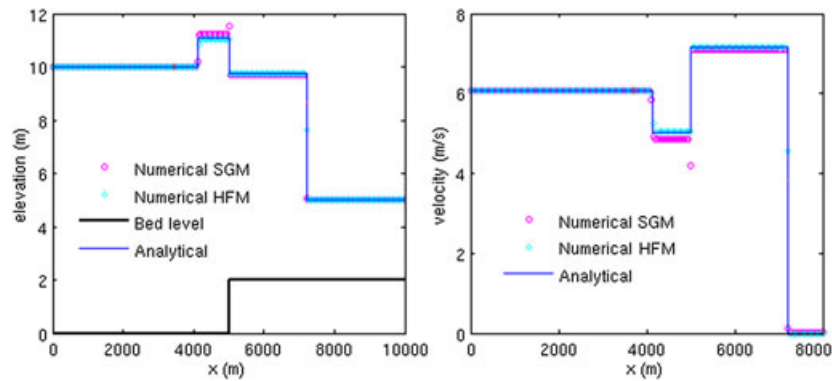


Figure 11. Comparisons of water surface and velocity between numerical and analytical solution at $t = 600.5$ s.

5.4. Dam-break flow over channel with a triangular bump

This case is used to test the numerical model with irregular bed topography for the wetting/drying problem. The laboratory dam-break flow over a triangular hump is reproduced in this section, as investigated by the European Union Concerted Action on Dam Break Modelling (EU CADAM) project [37]. The experimental setup is depicted in Figure 12, in which the lengths of bed profile and dam location are shown in which a symmetric triangular hump of 0.4 m is present. The still water surface elevation of the reservoir is 0.75 m upstream of the dam, although it is initially dry in the downstream floodplain of dam location. The downstream outlet of the domain is an open free outfall. Seven monitoring gauges are set up at 2 m, 4 m, 8 m, 10 m, 11 m, 13 m and 20 m downstream of the dam, respectively. The Manning coefficient n is set equal to 0.0125 throughout the domain, and the domain is discretised by $\Delta x = 0.04$ m. The simulation is run for 90 s, and the comparisons between numerical results and experimental data at Gauge 1, 3, 4, 5, 6 and 7 are given in Figure 13. The comparisons show that the predictions of arrival time and water depth have good agreement with measurement data at Gauge 1 to 6. However, at Gauge 7, after the bump, a discrepancy of water depth appears, but the arrival time is still well-predicted. Similar results were also obtained by other researchers [29, 35]. This discrepancy is thought to be due to a combination of numerical errors and measurement errors. Furthermore, the SGM approach is also implemented to reproduce this case and the comparisons are shown in Figure 12. At most gauges, the two simulated results do not have a large discrepancy except for Gauge 6 where the irregular bed is located. The proposed method achieves better results at Gauge 6 compared with those of SGM. This test shows the excellent stability and efficiency of proposed numerical model when modelling flow over an irregular bed in a wetting/drying case.

5.5. Two-dimensional shallow water sloshing in parabolic basin

This test was proposed by Thacker [38] who presented several analytical solutions to time-dependent periodic oscillations in parabolic basins. This benchmark is in two dimensions and represents a

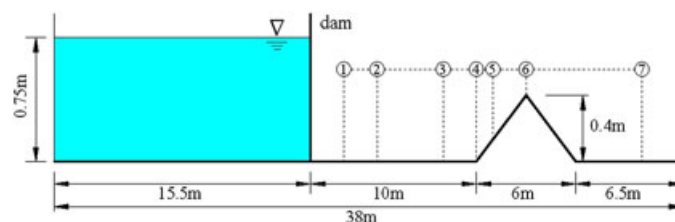


Figure 12. Dam-break flow over a triangular hump.

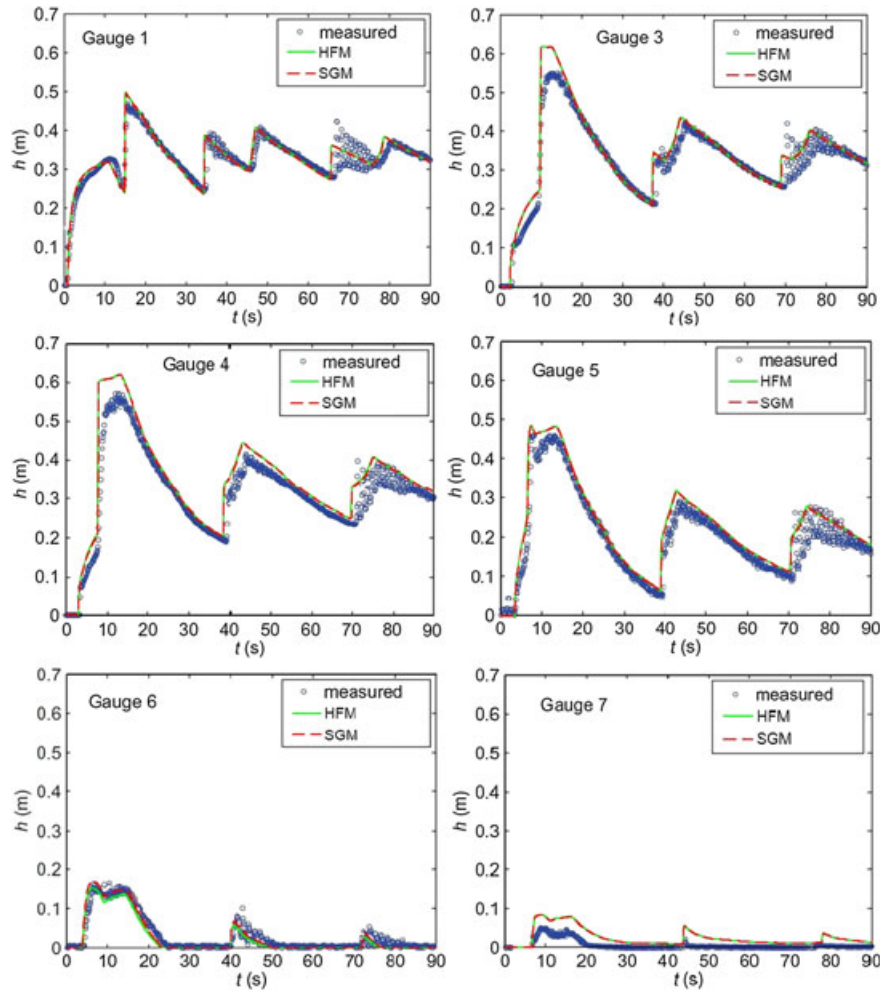


Figure 13. Dam break over a hump: time histories of water depth at different gauges, in which the solid line represents simulation results and cycle points for experimental measures.

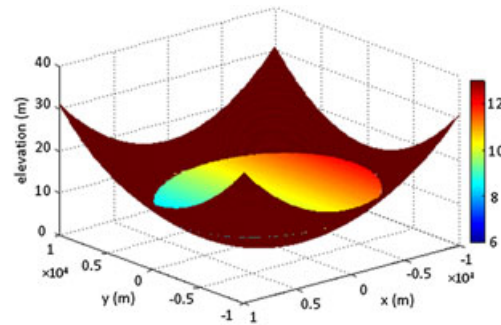
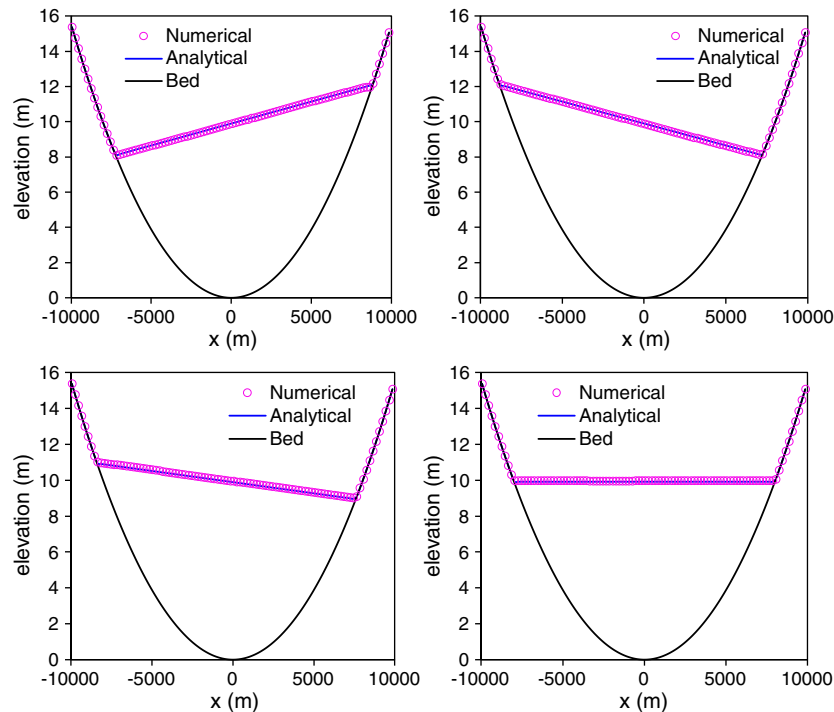
complex test case for the verification of a moving boundary problem solver with 2D wetting/drying fronts. In this case, a planar water surface profile circulates inside a parabola of revolution. The bed elevation of two-dimensional parabolic basin can be expressed by

$$z_b(x, y) = \frac{h_0}{a^2}(x^2 + y^2) \quad -10\,000 \text{ m} \leq x, y \leq 10\,000 \text{ m},$$

where h_0 is the water depth at the centre of the basin, and a is the distance from the centre to the shoreline with zero elevation. $h_0 = 10\text{m}$; $a = 8,025.5\text{m}$ in this study. The exact periodic solution can be expressed as the following water surface and velocity profile [38]:

$$\begin{aligned} z_w(x, y, t) &= \frac{\eta h_0}{a^2} [2x \cos(wt) + 2y \sin(wt) - \eta] + h_0, \\ u &= -\eta w \sin(wt), \\ v &= -\eta w \cos(wt), \end{aligned}$$

where η is a constant that determines the amplitude of the motion, $\eta = a/10 = 802.55$; $w = (2gh_0)^{0.5}/a = 2\pi/T$ is the frequency with periodic $T = 3600$ s. The parameter settings proposed by Liang [39] are applied here.

Figure 14. 3D view of water surface and bed profile at $t = T + T/2$.Figure 15. Comparisons between numerical solution and analytical solution proposed by Thacker [38] (The time is T , $T + T/2$, $2T + T/3$ and $2T + 3T/4$, respectively).

The computational domain is $20,000 \times 20,000$ m, which is discretised as 200×200 uniform cells ($\Delta x = \Delta y = 100$ m). The initial water surface profile at $t = 0$ is determined according to Equation (13). We run the proposed model on this test case for three periods. Figure 14 illustrates the 3D view of water surface at $t = T + T/2$, which is relatively smooth in the two-dimensional parabolic basin. We compare the numerical solutions and analytical solutions at $t = T, T + T/2, 2T + T/3$ and $2T + 3T/4$, respectively, which are demonstrated in Figure 15. The comparisons show a good agreement, with the proposed HFM approach able to track the wet/dry front interface extremely well. The velocity component in x -direction against time at point (5050, -50) and point (7950, -50) over the three periods is illustrated in Figure 16, which displays the comparisons between analytical solutions and numerical solutions. It is clear that good agreement is achieved. Furthermore, at $t = 2T + 3T/4$, the velocity u in x -direction and v in y -direction are also compared against Thacker's [38] analytical solutions (see Figure 17). The sensitivity analysis of tolerance water depth was carried out, and the results show that this threshold value does not affect the simulated results significantly. In general, the agreement is good, although some error points still occur

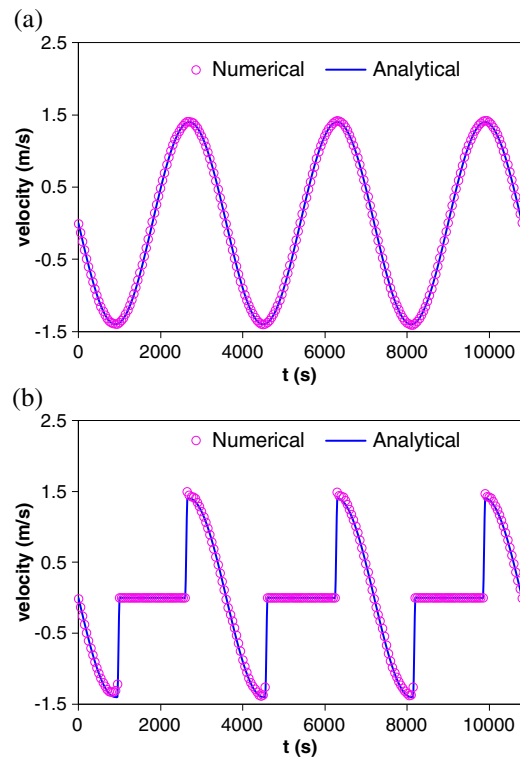


Figure 16. Comparison between numerical and analytical velocity in x -direction at point (a) (5050, -50) and (b) (7950, -50).

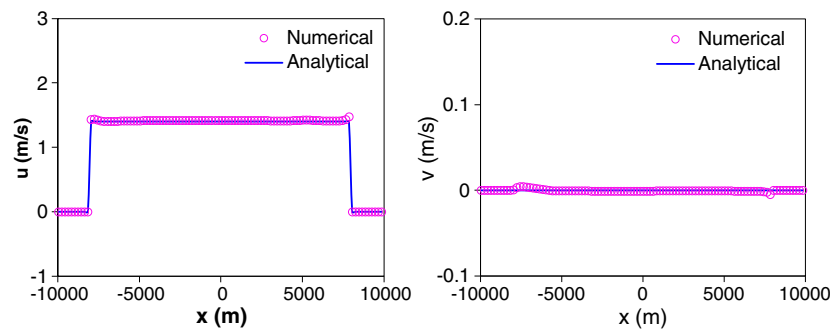


Figure 17. Comparison between numerical and analytical solutions of velocity in x -direction and y -direction against x -distance.

around the wet/dry interface area. In conclusion, this benchmark verifies the capability of the proposed numerical model and indicates that the model can cope well with unsteady flow and 2D wetting and drying over complex bed topography.

5.6. Dam-break flow around a 90° bend

The EU CADAM project conducted experiments [40] of dam-break flow through a 90° bend. The experiments facilities consisted of a square reservoir of $2.44 \text{ m} \times 2.39 \text{ m}$ and an L-shaped channel, which is depicted in Figure 18; in the L-shaped channel, bed level is set to 0 m; however, the bed level of the reservoir is -0.33 m, which forms a vertical step at the entrance to the channel. In the experiments, the initial water level in the reservoir is 0.2 m; in terms of water level in L-shaped channel, dry bed and wet bed cases in the L-shaped channel are taken into consideration;

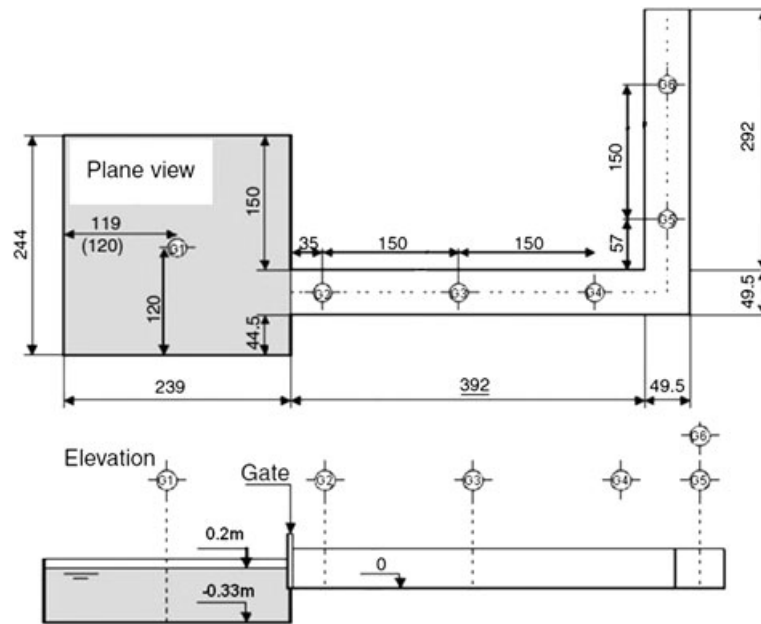


Figure 18. Geometry of the reservoir and L-shaped channel.

the water level for dry bed case is 0 m, whereas it is 0.01 m for wet bed case; the six measurement points are located at G1 (1.19 m, 1.21 m), G2 (2.74 m, 0.69 m), G3 (4.24 m, 0.69 m), G4 (5.74 m, 0.69 m), G5 (6.56 m, 1.51 m) and G6 (6.56 m, 3.01 m), taking the lower left corner as the origin. Manning's coefficient for the bed was set to 0.013. With respect to the numerical model for this case, the second-order TVD-WAF numerical scheme is applied here, and the computational grid is discretised as ($\Delta x = 0.04$ m, $\Delta y = 0.02$ m). For the flow process, the water flow arrives at the bend at approximately 3 s after the dam break; then, the water is reflected from the wall to form a bore, which propagates back towards the reservoir; whereas the water flow after the bend travels further downstream, multiple reflections on the walls can be observed and an eddy forms at the bend of channel. The comparisons between numerical results and measured data for dry and wet bed case at the measurement gauges are presented in Figure 19, which shows that the arrival time of the flow agrees well at all the gauges, and that water level at Gauge 3, 4 and 6 shows good agreement. However, the numerical water level at Gauge 5 after 20 s shows a bigger difference against experiment data. Such behaviour is also observed by other researchers [12, 41, 42]. The disagreement could, on the one hand, be due to additional head loss not accounted for in the numerical model causing higher numerical results; on the other hand, measurement error may also be a cause. Overall, the agreement is good, demonstrating the capability and the accuracy of the method for predicting dam-break flows over a vertical step.

5.7. Applied to glacial outburst flood at Sólheimajökull, Iceland

A volcano-induced glacial outburst flood occurred unexpectedly at Sólheimajökull, Iceland in July, 1999. It was well-documented and has been physically investigated in some significant detail [43, 44]. The purpose of this case is to elucidate whether the proposed numerical model is capable of simulating real extreme flood events by handling challenging wetting/drying over the complex irregular topography. Sólheimajökull is an 8-km long temperate, nonsurging outlet glacier draining the Mýrdalsjökull ice cap belonging to southern volcanic zone in southern Iceland. After the volcano erupted, the ice was melted by the high temperatures resulting in a high magnitude flood that occurred suddenly. The discharge increased from zero to 2000 m³/s in 1 h. The river channel is about 9 km long and around 400-700 m wide. Figure 20 illustrates the reconstructed cumulative

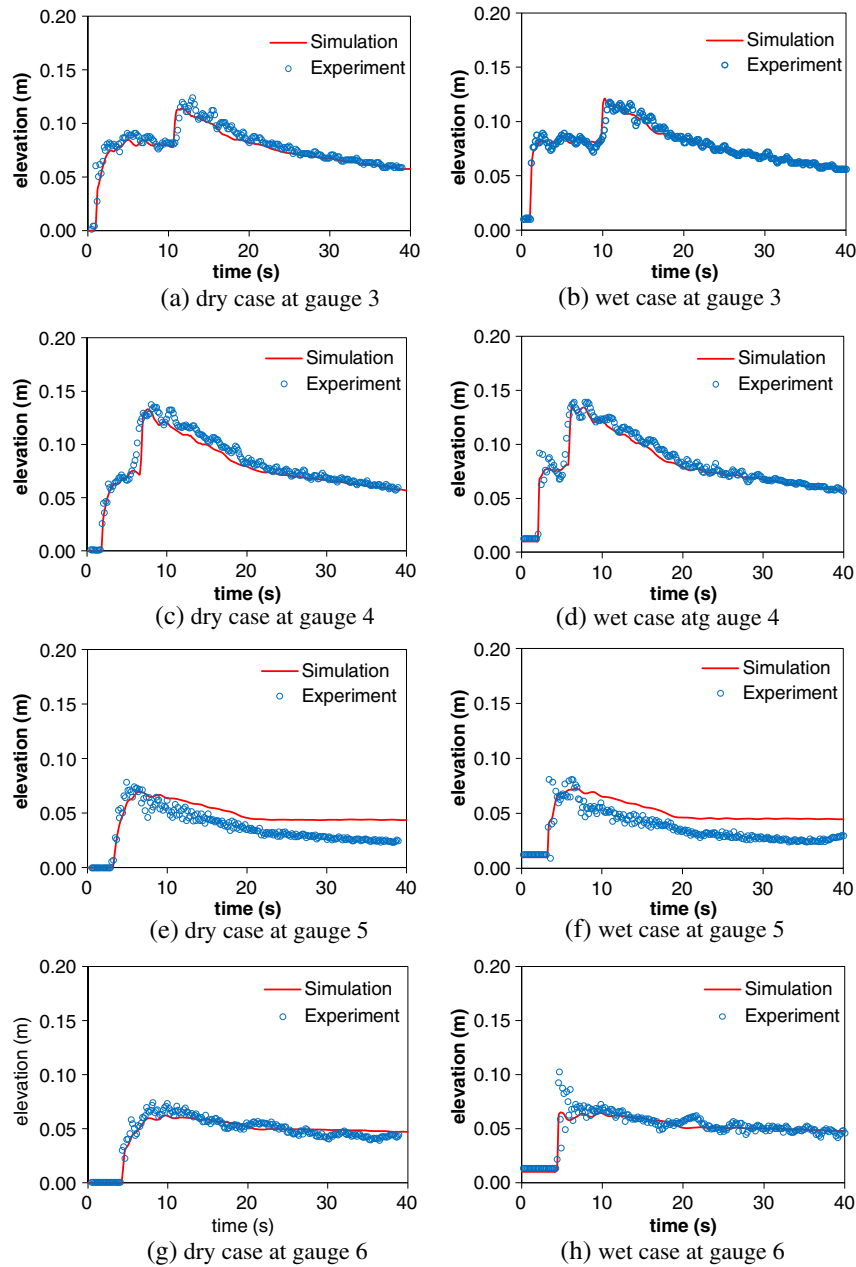


Figure 19. Comparisons between numerical and experimental data for dry and wet cases at Gauge 3 to 6; circular points represent experiment data and red lines are simulation results.

inflow hydrography from the two conduits, ignoring the flow from smaller outlets at the eastern margin. According to the field observation, sediment transport accompanied the sudden flood process; but in this case, we ignore the sediment transport effects, which are not our concern. The Manning's coefficient n is estimated according to Equation [44] as:

$$n = 0.038d_{90}^{1/6},$$

where d_{90} is the 90th percentile bed grain-size values.

The inflow boundary is described by a 6h inflow hydrograph as shown in Figure 20; the outflow boundary is set as open. The topography is defined by a 8×8 m resolution height-based dataset,

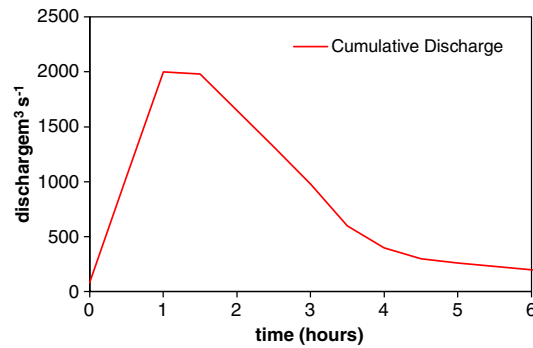


Figure 20. The cumulative inflow hydrograph from Western Conduit, Central Conduit.

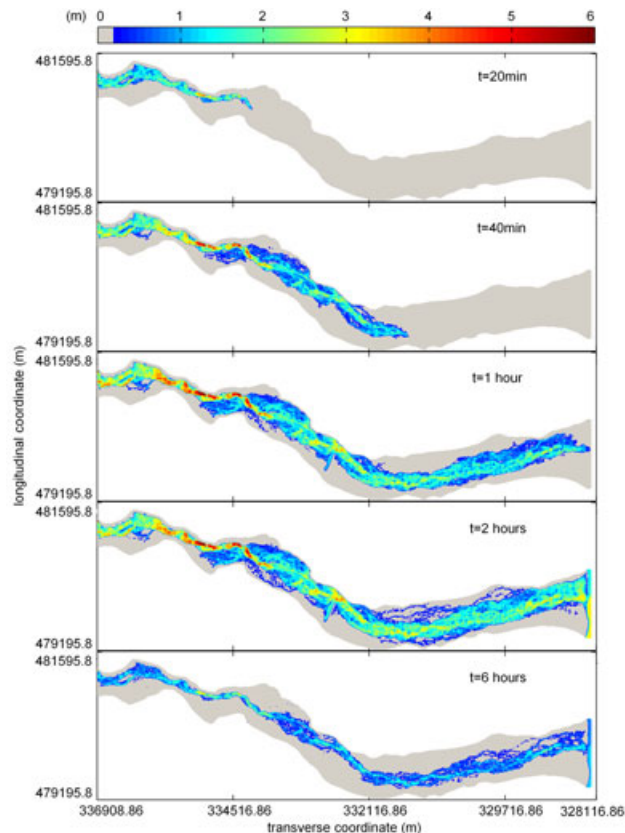


Figure 21. The spatial and temporal change of the flood water depth at $t = 20$ min, 40 min, 1 h, 2 h and 6 h after the flood occurred.

and the computational area is discretized by a grid of 1089×287 cells. During the simulation, the Courant number is fixed as 0.5, and the time interval varies with each computational step to satisfy this condition. In addition, initially, the whole domain is considered dry. Figure 21 shows the spatial and temporal change of the flood water depth during the simulation. A bridge and gauge exist at position (332908.86, 480099.78); this point is used as the location at which to compare discharges and water levels. These results are illustrated in Figure 22. It can be seen that the flood water arrives at the bridge location after approximately 30 min and the peak discharge arrives about 1 h and 20 min after the flood occurs. As the release of water is very sudden, the level increases to a maximum depth very rapidly, the water level then decreases progressively as the level in the volcanic lake is reduced. The extent of the flood inundation reduces correspondingly as shown in

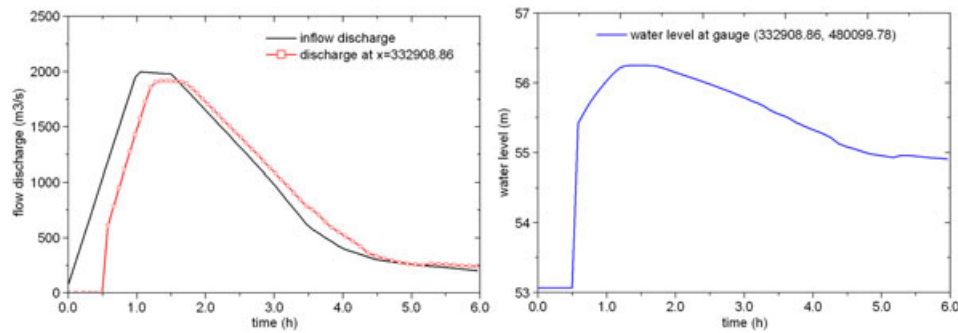


Figure 22. The discharge against time at the cross section nearby the bridge location ($x = 332908.86$) and the water level at the gauge (332908.86, 480099.78).

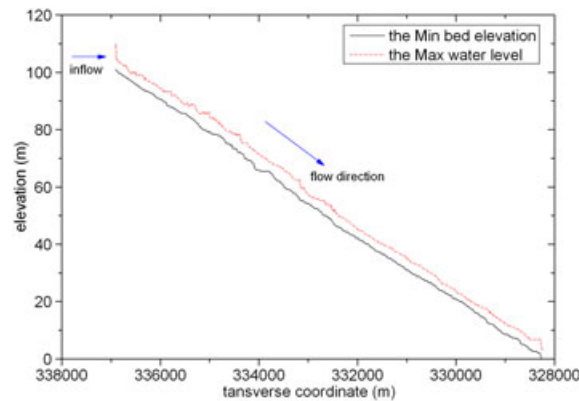


Figure 23. The maximum water surface and the minimum bed level in the entire river channel.

Figure 21. At about 2 h, the flood waters cover a significant portion of the domain, the maximum water surface and minimum bed elevation at each cross section are illustrated in Figure 23. The maximum water depth in the channel is approximately 3 to 6 m with an average depth of 4.07 m. Because of the lack of hydraulic data, a comparison with measured data is not carried out. However, this test demonstrates that the proposed numerical model can simulate the kind of high magnitude outburst flood, which necessitates the addressing of flow over complex irregular topography.

6. CONCLUSIONS

This paper presents a 2D shallow water model with a robust HFM source term treatment and a simply implemented wetting/drying method for flows over irregular bed topography. The HFM source term treatment method incorporates the bed slope term into the flux gradient, which automatically maintains the flux balance. A second-order TVD-WAF finite volume scheme is applied to solve the governing equations. The proposed model is verified by several benchmark tests and experimental results from the EU CADAM project. The method is also applied to simulate an extreme flow case of a real-world flood with complex irregular topography. The proposed numerical scheme has the following advantages and robust characteristics:

- it is straightforward to implement,
- it copes with discontinuous or vertical bed topography as a matter of course without any special treatment,
- it is applicable to both steady and unsteady shallow water flow problems over complex irregular topography.

The proposed model in the study considers only water flow. In practice, it is common that sediment particles would be entrained and transported in these flows. The interaction between flow and sediment render it necessary to incorporate sediment effects into the robust well-balanced hydrodynamic model. Further work is focused on this extension.

ACKNOWLEDGEMENTS

The first author would like to thank the China Scholarship Council (CSC) and the School of Civil Engineering at University of Leeds for their financial support for his PhD studies. Furthermore, thanks for the data of Iceland flood case provided by Dr. Carrivick, School of Geography, University of Leeds.

REFERENCES

1. Stelling GS. *On the Construction of Computational Methods for Shallow Water Flow Problems*, in *Applied Sciences*. Government Pub. Office: Hague, The Netherlands, 1983.
2. Falconer RA. *Mathematical Modelling of Jet-Forced Circulation in Reservoirs and Harbours*. University of London: London, 1976.
3. van Leer B. Towards the ultimate conservative difference scheme. V. A second-order sequel to Godunov's method. *Journal of Computational Physics* 1979; **32**(1):101–136.
4. Sleigh PA, Gaskell PH, Berzins M, Wright NG. An unstructured finite-volume algorithm for predicting flow in rivers and estuaries. *Computers & Fluids* 1998; **27**(4):479–508.
5. Alcrudo F, Garcia-Navarro P. A high-resolution Godunov-type scheme in finite volumes for the 2D shallow-water equations. *International Journal for Numerical Methods in Fluids* 1993; **16**:489–505.
6. Begnudelli L, Sanders BF. Unstructured grid finite-volume algorithm for shallow-water flow and scalar transport with wetting and drying. *Journal of Hydraulic Engineering* 2006; **132**(4):371–384.
7. Bermudez A, Vazquez E. Upwind methods for hyperbolic conservation-laws with source terms. *Computers & Fluids* 1994; **23**(8):1049–1071.
8. Garcia-Navarro P, Vazquez-Cendon ME. On numerical treatment of the source terms in the shallow water equations. *Computers & Fluids* 2000; **29**(8):951–979.
9. LeVeque RJ. Balancing source terms and flux gradients in high-resolution Godunov methods: the quasi-steady wave-propagation algorithm. *Journal of Computational Physics* 1998; **146**(1):346–365.
10. Nujic M. Efficient implementation of non-oscillatory schemes for the computation of free-surface flows. *Journal of Hydraulic Research* 1995; **33**(1):101–111.
11. Zhou JG, Causon DM, Mingham CG, Ingram DM. The surface gradient method for the treatment of source terms in the shallow-water equations. *Journal of Computational Physics* 2001; **168**(1):1–25.
12. Zhou JG, Causon DM, Ingram DM, Mingham CG. Numerical solutions of the shallow water equations with discontinuous bed topography. *International Journal for Numerical Methods in Fluids* 2002; **38**(8):769–788.
13. Lee S-H, Wright NG. Simple and efficient solution of the shallow water equations with source terms. *International Journal for Numerical Methods in Fluids* 2010; **63**(3):313–340.
14. Brufau P, Garcia-Navarro P, Vazquez-Cendon ME. Zero mass error using unsteady wetting-drying conditions in shallow flows over dry irregular topography. *International Journal for Numerical Methods in Fluids* 2004; **45**(10):1047–1082.
15. Liang QH, Borthwick AGL. Adaptive quadtree simulation of shallow flows with wet–dry fronts over complex topography. *Computers & Fluids* 2009; **38**(2):221–234.
16. Bradford SF, Sanders BF. Finite-volume model for shallow-water flooding of arbitrary topography. *Journal of Hydraulic Engineering* 2002; **128**(3):289–298.
17. Song L, Zhou J, Guo J, Zou Q, Liu Y. A robust well-balanced finite volume model for shallow water flows with wetting and drying over irregular terrain. *Advances in Water Resources* 2011; **34**(7):915–932.
18. Toro EF. *Shock-capturing Methods for Free-surface Shallow Flows*. John Wiley: Chichester, New York, 2001.
19. Toro EF. Riemann Problems and the WAF Method for solving the two-dimensional shallow water equations. *Philosophical Transactions: Physical Sciences and Engineering* 1992; **338**(1649):43–68.
20. Fernández-Nieto ED, Narbona-Reina G. Extension of WAF type methods to non-homogeneous shallow water equations with pollutant. *Journal of Scientific Computing* 2008; **36**(2):193–217.
21. Toro EF. A weighted average flux method for hyperbolic conservation laws. *Proceedings of the Royal Society of London. Series A, Mathematical and Physical Sciences* 1989; **423**(1865):401–418.
- 22.infeldt B. On Godunov-type methods for gas-dynamics. *Siam Journal on Numerical Analysis* 1988; **25**(2):294–318.
23. Audusse E, Bristeau M-O. A well-balanced positivity preserving “second-order” scheme for shallow water flows on unstructured meshes. *Journal of Computational Physics* 2005; **206**(1):311–333.
24. Gallardo JM, Parés C, Castro M. On a well-balanced high-order finite volume scheme for shallow water equations with topography and dry areas. *Journal of Computational Physics* 2007; **227**(1):574–601.
25. Vazquez-Cendon ME. Improved treatment of source terms in upwind schemes for the shallow water equations in channels with irregular geometry. *Journal of Computational Physics* 1999; **148**(2):497–526.

26. Sanders BF. Integration of a shallow water model with a local time step. *Journal of Hydraulic Research* 2008; **46**(4):466–475.
27. Crossley AJ, Wright NG. Time accurate local time stepping for the unsteady shallow water equations. *International Journal for Numerical Methods in Fluids* 2005; **48**(7):775–799.
28. Kramer T, Jozsa J. Solution-adaptivity in modelling complex shallow flows. *Computers & Fluids* 2007; **36**(3):562–577.
29. Brufau P, Vazquez-Cendon ME, Garcia-Navarro P. A numerical model for the flooding and drying of irregular domains. *International Journal for Numerical Methods in Fluids* 2002; **39**(3):247–275.
30. Brufau P, García-Navarro P. Unsteady free surface flow simulation over complex topography with a multidimensional upwind technique. *Journal of Computational Physics* 2003; **186**(2):503–526.
31. Kesserwani G, Liang Q. Well-balanced RKDG2 solutions to the shallow water equations over irregular domains with wetting and drying. *Computers & Fluids* 2010; **39**(10):2040–2050.
32. Caleffi V, Valiani A, Zanni A. Finite volume method for simulating extreme flood events in natural channels. *Journal of Hydraulic Research* 2003; **41**(2):167–177.
33. Goutal N, Maurel F. Proceedings of the 2nd workshop on dam-break wave simulation. HE 43/97/016/B, Département Laboratoire National d'Hydraulique, Groupe Hydraulique Fluviale Electricité de France, France, 1997.
34. Rogers BD, Borthwick AGL, Taylor PH. Mathematical balancing of flux gradient and source terms prior to using Roe's approximate Riemann solver. *Journal of Computational Physics* 2003; **192**(2):422–451.
35. Liang Q, Marche F. Numerical resolution of well-balanced shallow water equations with complex source terms. *Advances in Water Resources* 2009; **32**(6):873–884.
36. Hu K, Mingham CG, Causon DM. Numerical simulation of wave overtopping of coastal structures using the non-linear shallow water equations. *Coastal Engineering* 2000; **41**(4):433–465.
37. Morris M. *CADAM: Concerted Action on Dam Break Modeling—Final report*, in Report SR 571. HR Wallingford Limited: HR Wallingford, 2000.
38. Thacker W. Some exact solutions to the nonlinear shallow-water wave equations. *Journal of Fluid Mechanics* 1981; **107**:499–508.
39. Liang QH. Flood simulation using a well-balanced shallow flow model. *Journal of Hydraulic Engineering* 2010; **136**(9):669–675.
40. Soares Frazao S, Zech Y. Dam break in channels with 90 degrees bend. *Journal of Hydraulic Engineering-Asce* 2002; **128**(11):956–968.
41. Zhou JG, Causon DM, Mingham CG, Ingram DM. Numerical prediction of dam-break flows in general geometries with complex bed topography. *Journal of Hydraulic Engineering-Asce* 2004; **130**(4):332–340.
42. Soares Frazão S, Sillen S, Zech Y. Dam-break flow through sharp bends: physical model and 2D Boltzmann model validation. *Proceedings of the CADAM Meeting*, Wallingford, UK, 1998; 151–169.
43. Russell AJ, Tweed FS, Knudsen Ó. Flash flood at Sólheimajökull heralds the reawakening of an Icelandic subglacial volcano. *Geology Today* 2000; **16**(3):102–106.
44. Russell AJ, Tweed FS, Roberts MJ, Harris TD, Gudmundsson MT, Knudsen ÓMarren PM. An unusual jökulhlaup resulting from subglacial volcanism, Sólheimajökull, Iceland. *Quaternary Science Reviews* 2010; **29**(11–12):1363–1381.